International Journal of Fatigue 199 (2025) 109015



Contents lists available at ScienceDirect

International Journal of Fatigue

journal homepage: www.elsevier.com/locate/ijfatigue





Experimental investigation of fatigue crack propagation under non-proportional multiaxial loading

Bemin Sheen, Catrin Davies, David Nowell *

Imperial College London, Exhibition Road, London, SW7 2AZ, UK

ARTICLE INFO

Keywords:
Fatigue
Multiaxial
Non-proportional
Crack propagation

ABSTRACT

Blisks (bladed disks) are critical components in modern aero-engines that offer significant weight savings compared to conventional blade and disk rotor designs, resulting in improved fuel efficiency. However, due to their integrated design, blisks are susceptible to unique failure modes following foreign object damage (FOD) and crack initiation. Of particular interest is the trajectory of crack propagation from FOD sites, which determines whether failure will occur via a blade-off event or rupture of the blisk.

This work presents an experimental test setup which replicates the key features of non-proportional loading in a blisk. A novel feature of the test rig was the ability to apply loads independently in three axes using a biaxial machine equipped with only two hydraulic servo-actuators. A series of multiaxial fatigue tests were completed on notched cruciform specimens and a wide range of crack trajectories were achieved, validating the design of the test rig.

Crack trajectories produced by non-proportional load paths are not accurately predicted by conventional criteria, such as the maximum tensile stress criterion (MTS), when cracks are subject to high mean mode-II loads. The results of these experiments underscore the complexity of modelling non-proportionally loaded cracks and the acquired crack trajectory data is a useful tool for validating further models.

1. Introduction

Bladed disks (or blisks) are a modern development in aero-engines. Traditional rotor designs are comprised of a central disk with blades which attach via a mechanical joint such as a dovetail root. A blisk integrates the blades and disk into one solid body. The removal of dovetail joints removes a point of failure and reduces the bulk at the disk rim. This allows for more aerodynamically efficient and lighter designs, which translate into an increase in fuel efficiency.

In traditional blade and disk rotor designs, a common mode of failure is fatigue crack growth initiating from the dovetail joint. Crack initiation by fretting results from the small tangential movement of the one surface of the joint relative to another. Propagation of a crack through a blade, via blade vibration, results in a blade-off event. While engine cases are designed to contain a blade during blade-off testing, this may still result in extensive damage to an engine. Crack propagation through a disk may result in a disk failure, which engines are not designed to contain. Ruptured disks cause catastrophic failures to aircraft as they may penetrate the fuselage or other engines.

Despite the point of failure, the dovetail joint can also provide some natural damping to the system, which reduces the amplitude of forcing. Repair can be simpler due to the modular nature of the blade and disk requiring only the damaged part to be replaced. The joint will also prevent a crack originating from a blade to grow into the disk. Since the disk is a more critical part, this natural form of crack arrest is a benefit.

Without the dovetail joint, the blade portion of blisks are subject to greater levels of vibration and a crack is not prevented from initiating in the blade portion and growing towards the centre of the disk. Crack initiation in blisks typically results from foreign object damage (FOD). It has been observed from blisks which have been subject to FOD in service, that a crack which initiates on the blade will typically propagate across the blade and result in a blade-off. However, if the initiation site is located in the fillet regions of the blade and disk, as shown in Fig. 1, there is a risk of propagation into the disk.

1.1. Objectives

Current criteria for determining whether a FOD site poses a risk of initiating a crack with a dangerous trajectory are simple and highly conservative. In order to improve on existing criteria, further understanding of non-proportionally loaded cracks is required through improved

* Corresponding author.
E-mail address: d.nowell@imperial.ac.uk (D. Nowell).

https://doi.org/10.1016/j.ijfatigue.2025.109015
Received 27 January 2025; Received in revised form 10 April 2025; Accepted 21 April 2025
Available online 3 May 2025
0142-1123/© 2025 The Authors. Published by Elsevier Ltd. This is an open access article under the CC BY license (http://creativecommons.org/licenses/by/4.0/).

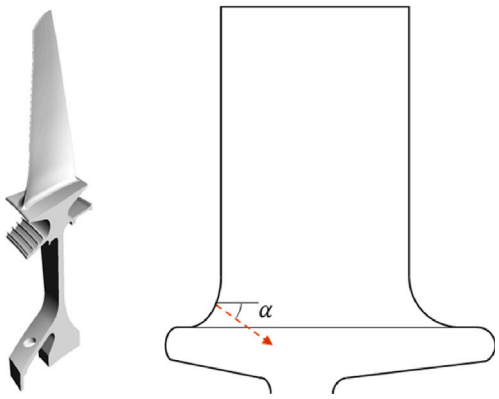


Fig. 1. Sector of a blisk with crack initiating in the fillet region.

computational methods and experimental validation. To approach this problem, a series of experiments has been completed under a range of controlled conditions to establish practical growth trajectories.

2. Literature

2.1. Multiaxial loading

Whilst early crack growth models were effective for predicting growth in mode-I, cracks in real structures are subjected to a combination of mode-I, II and III loads which each produce stress intensity factors K_I, K_{II} and K_{III}. Long cracks loaded in mode-I are expected to grow in a direction which is perpendicular to the direction of loading. However, introducing mode-II loading may change the direction to a degree which is dependent on the material. When predicting crack trajectories, the mode-mixity expressed as $\tan\phi = K_{II}/K_I$, is a useful variable to introduce. K_{III} is omitted and is considered to have a lesser effect on the crack trajectory [1] although it may have a significant effect on growth rate. Loading is considered to be proportional if the mode-mixity remains constant during a cycle. Existing crack growth criteria such as the maximum tensile stress criterion (MTS, also referred to as the maximum tangential stress criterion) and maximum shear stress criterion (MSS) are able to provide accurate predictions proportionally loaded for 2D cracks in certain materials. Comprehensive reviews of mixed-mode fatigue crack growth criteria can be found in [2–4].

2.2. Maximum tensile stress criterion

The MTS criterion, proposed by Erdogan and Sih [5], assumes that crack growth occurs in the direction which is perpendicular to the maximum tangential stress $\sigma_{\theta\theta}$ at the crack tip. The tangential stress around the crack tip may be expressed in terms of SIFs as shown in Eq. (1) [6].

$$\sigma_{\theta\theta} = \frac{K_I}{\sqrt{2\pi r}}\left(\frac{3}{4}\cos\frac{\theta}{2} + \frac{1}{4}\cos\frac{3\theta}{2}\right) + \frac{K_{II}}{\sqrt{2\pi r}}\left(-\frac{3}{4}\sin\frac{\theta}{2} - \frac{3}{4}\sin\frac{3\theta}{2}\right) \quad (1)$$

It is assumed that tangential stress will be at a maximum at the critical angle of crack growth, θ_c. So at this point, the derivative may be set to zero: $\partial\sigma_{\theta\theta}/\partial\theta = 0$. Differentiating and simplifying yields Eq. (2). When finding the solution at the maximum, the trivial solution of $\theta_c = 180°$ may be discarded.

$$\frac{\partial\sigma_{\theta\theta}}{\partial\theta} = \cos\frac{\theta}{2}[K_I\sin\theta + K_{II}(3\cos\theta - 1)] \quad (2)$$

Thus θ_c is found by solving Eq. (3). One form of the solution is presented in Eq. (4) although several alternate forms of the equation exist. A visualisation of the effect of K_{II} on the growth angle is seen in Fig. 2. No deflection results from $K_{II} = 0$ and if $K_{II}/K_I = \pm\infty$, $\theta_c = \mp\arccos(1/3) = \mp 70.5°$.

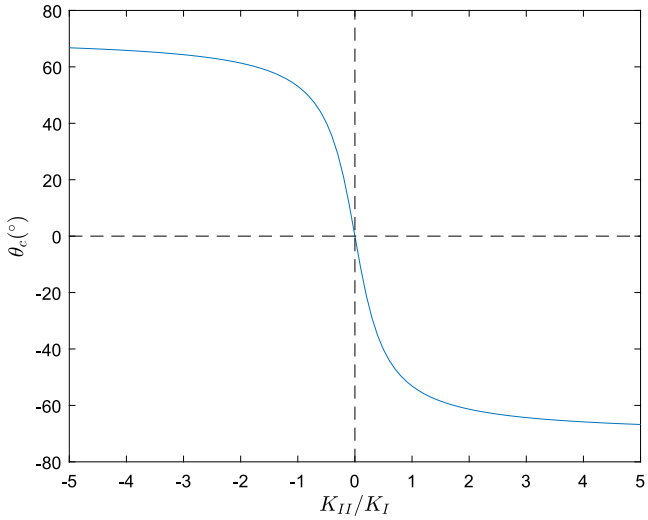


Fig. 2. Relationship between θ_c and mode-mixity.

$$0 = K_I\sin\theta_c + K_{II}(3\cos\theta_c - 1) \quad (3)$$

$$\theta_c = \arcsin(K_{II}/\sqrt{K_I^2 + 9K_{II}^2}) + \arctan(3K_{II}/K_I) \quad (4)$$

After a crack deflects according to MTS, the new crack trajectory will be aligned in the direction which maximises ΔK_I and minimises ΔK_{II} [3,7].

2.3. Non-proportional loading

Non-proportional loading is a specific case of multiaxial loading. It occurs when a crack is loaded in a mixed-mode scheme where the mode-mixity varies during a cycle. This results in the directions of the principal stresses rotating, which causes increased damage within a cycle, so criteria based on ΔK calculated from K_{max} and K_{min} alone are inaccurate. The in-cycle changing in the stress directions also increases the rate of cyclic hardening, which accelerates crack growth. Many experiments and simulations have been performed to find a non-proportional cyclic hardening coefficient which can be factored into existing damage criteria [8–10]. However, experimental findings have also shown that an increase cyclic hardening from non-proportional loading is not always the cause of the increased growth rate [11].

Many authors have performed non-proportional loading experiments using tension-torsion specimens to apply mode-I and mode-II independently. Fatemi and Shamsaei [12] completed a series of fatigue tests on such test specimens. 90° Out-of-phase loading resulted in a higher crack growth rate and fewer cracks growing compared to in-phase loading. The higher growth rate was explained by a higher normal stress occurring on the maximum shear plane in out-of-phase loading. A similar result was obtained by Yu, Li and Proust [13] who observed mixed mode-I and II crack growth in tubular specimens of aluminium alloy 7076-T651. Thirteen non-proportional load cycles were tested. Additionally, the authors found that loading two specimens with load cycles which were identical but reversed in direction (clockwise and anti-clockwise) resulted in drastically different crack growth rates.

2.4. Fatigue crack growth modelling in aero-engine applications

Several attempts have been made at modelling crack growth in compressor blades. The work of Mangardich et al. [14] compares simulated crack growth in fractured compressor aerofoils using iterative

remeshing in the fracture analysis software, FRANC3D [15]. The aerofoils, made from Ti-6Al-4V, were subjected to low cycle fatigue (LCF) loads from rotation and heat, and high cycle fatigue (HCF) loads from bending. The authors concluded from fractographic analysis of aerofoil fracture surfaces that HCF was predominantly responsible for crack growth. Simulated cracks grown under only LCF loading did not match the fractured samples in direction or shape. The HCF crack growth was accelerated by the LCF load since it imposed a positive mean stress on the dynamic bending load, however the LCF cycles themselves did not make a significant contribution. The authors found that LEFM and the MTS criterion predicted the crack direction accurately which is in line with previous studies on crack growth in Ti-6Al-4V blades [16]. However, Mangardich notes that in many previous studies conducted on blades with dovetail attachments, damping reduces the effect of the vibratory stresses. Byrne et al. [17] identified that in Ti-6Al-4V specimens, a crack would initially propagate in LCF until the HCF threshold was reached. Overloading the specimen prior to dynamic loading reduced the effect of HCF.

A hybrid approach to modelling was used by Witek [18] to model a compressor blade subject to resonant vibration. The blade was modelled analytically using a simplified rectangular geometry and the Raju-Newman equations on a half elliptical crack. The model used a Paris growth law to estimate a 29% greater lifetime than the experimental results from the blade. The discrepancy may be explained by oversimplification of the blade geometry. The analytical model only considered crack growth when the blade was displaced to the pressure side which could also lead to a less conservative lifetime estimate.

A significant amount of work has been dedicated to modelling crack growth rates in aero-engine components, due to the nature of fatigue failure in these parts. Studies have also focussed on the interactions between low and high-cycle components of a loading block and their effect on the overall growth rate. Less attention has been given to accurately modelling crack trajectory in blisks, which therefore requires further investigation.

3. Experimental setup

Preliminary modelling of a blisk was completed before designing a test sample to represent the key features of crack propagation. An important factor affecting crack growth in the fillet region is the superposition of cyclic loads of different frequencies. A radial load and tangential load are present due to the rotational load from the rotation of the compressor. These are cycled when the engine is started and stopped. Blade vibration produces a combination of cyclic loads corresponding to different vibration modes. The first mode produces a bending moment at the base of the blade which is predominantly responsible for propagating the crack in high cycle fatigue. This bending load has a non-zero mean value due to the pressure difference across the blade.

Although loads in the blisk were categorised as steady or cyclic, some consideration was given to the infrequent cyclic variation of the rotation loads. Two simplified loading blocks were considered in the fatigue models and experiments. The loading block in Fig. 3a only considers the effect of superimposing a cyclic load onto a static load. Fig. 3b accounts for the infrequent cycling of the engine speed. Two hundred minor vibrations take place inside one flight block.

Typical crack paths in a blisk were modelled from initiation locations located at different heights on the blisk fillet. Modal analysis in ABAQUS was used to find the individual contributions of blade vibration and engine rotation in driving crack growth. A thorough explanation of the crack modelling procedure is provided in [19]. Three example sub-models of the filleted region are presented in Figs. 4–6 with initiation sites located at 25%, 50% and 100% of the height of the fillet region. At step 0, cracks were elliptical and on a plane inclined at 45° between radial and circumferential directions. The SIFs due to blade movement to the high pressure side during blade vibration are plotted for the initial crack growth steps. As expected when using the MTS model, the magnitude of K_{II} decreases with each step. Crack trajectories approximately follow expected trends as lower initiation locations result in more hoopwise crack growth. It is worth noting that the SIFs in Figs. 5 and 6 are close to lower bound estimates of the ΔK_{th} for Ti-6Al-4V [20].

Table 1
Load application per configuration.

Load	Configuration A	Configuration B
P_x	Machine horizontal actuator	Hydraulic cylinder
P_y	Machine vertical actuator	Machine vertical actuator
P_z	Hydraulic cylinder	Machine horizontal actuator

A cruciform specimen geometry was chosen for the ability to load it independently in two axes. The stress state in the centre of the cruciform around the internal corners may be controlled to replicate stresses in the filleted area of the blisk. Although the blade vibration is considered as a bending load, which generates tension in the thin shape of the blade, the shear stress at the bottom of the fillet is significant and can result in a significant K_{III} component. Therefore, it was seen as necessary to apply blade load through a similar bending setup instead of superimposing it on the rotational radial load.

During this test campaign, two configurations of loading were used. Fig. 7 depicts how the cruciform is loaded. P_x and P_z are representative of the radial and hoop load due to rotation respectively. P_y represents the vibrational load and is applied via a 4-point bending setup. The specimen is designed for a biaxial machine with two servo-controlled hydraulic actuators. A third loading axis has been added using a hydraulic cylinder which is pressurised using a hand pump. The loading on this axis may therefore only be held constant during tests. Two test rig configurations were used in this test series, which correspond to the flight blocks in Fig. 3. The application of load in each axis was performed as listed in Table 1. While non-proportional loading is used in both configurations, the loading in configuration A has a lower variation in mode-mixity during a cycle due to the cycling of only the bending load.

Similar cruciform designs were used for both test configurations. One pair of arms is longer to accommodate the 4-point bending setup. A schematic of both cruciform designs is provided in Fig. 8. The B configuration specimen is noticeably smaller. The size of loading point for P_x was reduced because it bore lower load from the hydraulic cylinder. The specimen was longer in the z-dimension in configuration A in order for the hydraulic fixture to fit around the 4-point bending loading pin assembly which is attached to the vertical actuator. In configuration B, this assembly was rotated by 90° which made it less obstructive to the hydraulic fixture and allowed the length of the cruciform to be reduced.

Cracks were inserted into the internal corners of the cruciform specimens. The loads and starter notch locations could be adjusted to alter the SIFs around the crack front. Two types of starter notches were used in the tests — through thickness notches and corner notches. Fig. 9 specifies the dimensions and locations of the notches. The notch angle, θ_N was 45° for most tests and notches were cut with an EDM wire of thickness 0.25 mm. In tests B5–B8, notch locations were altered to place the notch in a different stress field. The loading schemes and the number of notches for each test are summarised in Table 2. In specimens listed as having two edge notches (2E) or two corner notches (2C), notches were placed in opposite corners. In earlier tests, multiple notches were used to reduce the time to the first initiation. Later tests used a single notch to represent FOD in a blisk. Overall, nine steel specimens (S275) were used for preliminary tests and to verify the test rig. Thirteen Ti-6Al-4V specimens were then tested.

With this test geometry, cracks are driven by the cyclic bending load P_y which encourages crack growth normal to the x-direction. This is analogous to a crack in a blisk which grows across the blade while driven by vibration. Increasing P_z encourages the crack to deflect from

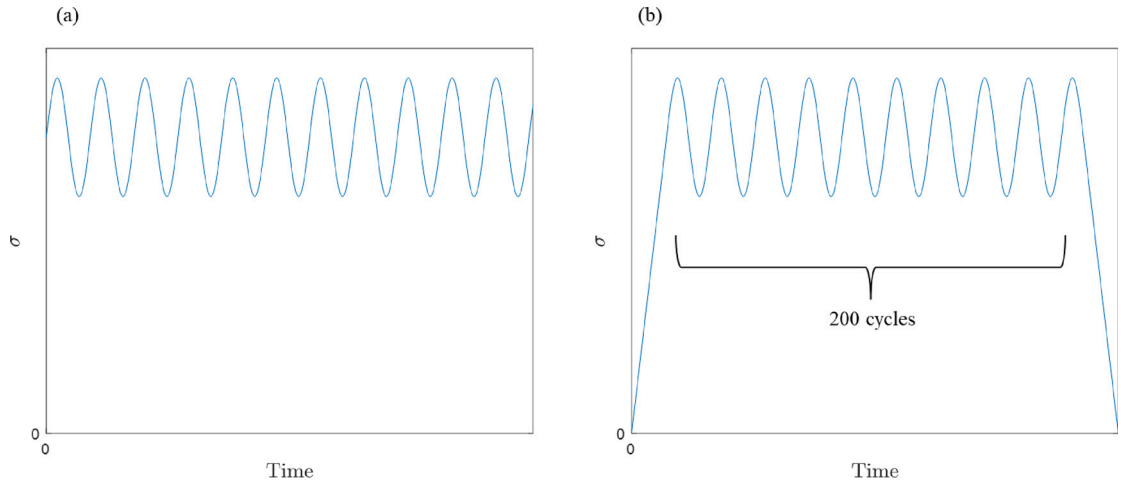


Fig. 3. Simplified flight blocks.

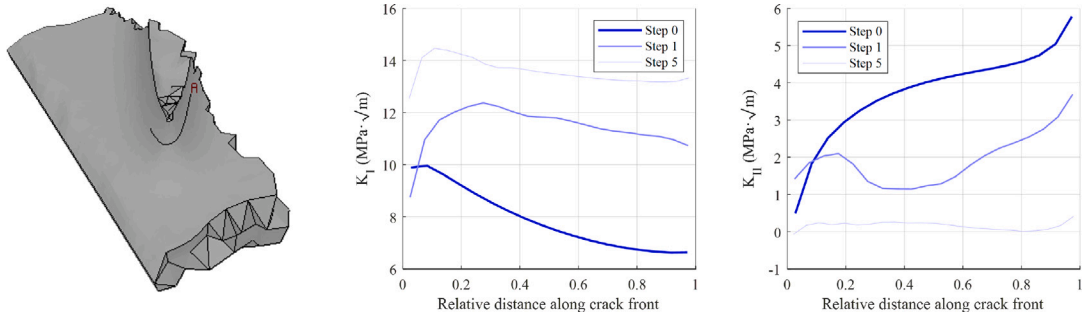


Fig. 4. Blisk with crack initiation at 100% fillet height, subject to blade vibration.

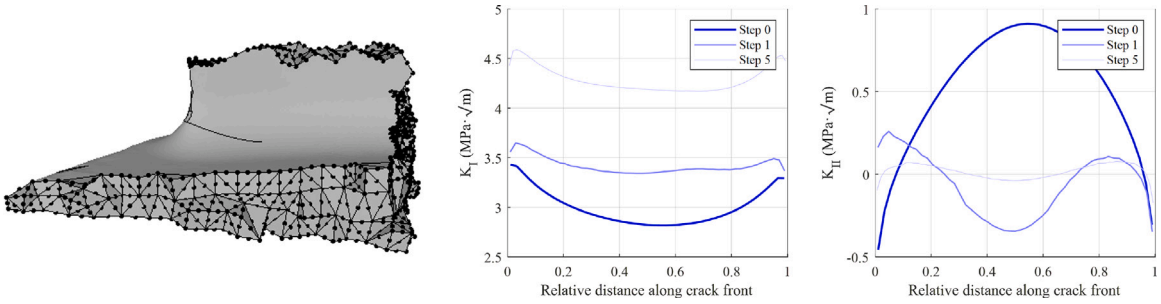


Fig. 5. Blisk with crack initiation at 50% fillet height, subject to blade vibration.

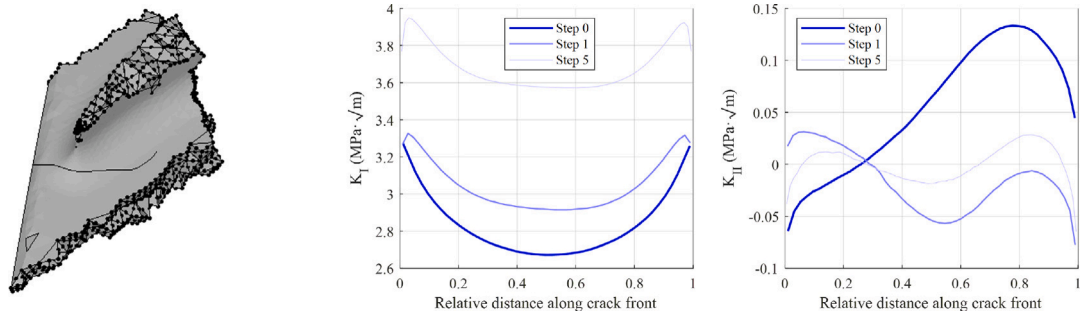


Fig. 6. Blisk with crack initiation at 25% fillet height, subject to blade vibration.

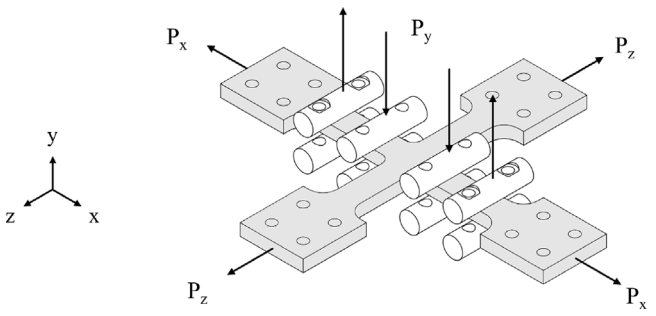


Fig. 7. Specimen in four point bending.

this direction and this is akin to the affect of hoop stresses turning a crack in a blisk towards the hoop direction. Crack growth normal to P_z is therefore analogous to a crack in a blisk growing 'hoopwise' towards the bore.

In both configurations, the vibrational load P_y required the use of a servo-controlled actuator. In configuration A, the hoop load was applied by the hydraulic cylinder and neither P_x or P_z were cycled. It was found early on in the test series that most cracks would grow almost normal to the direction of P_x, which is parallel to the direction of the bending stress applied to P_y. It was desirable to investigate a larger range of crack trajectories which required inducing a larger deflection. Therefore a second configuration of the rig was designed apply larger P_z loads using the horizontal actuator of the biaxial machine. In this configuration (B), P_z was also cycled once per block as in Fig. 3b with the aim of inducing more 'hoopwise' crack growth.

3.1. Test rig design

A model of the configuration A test rig is displayed in Fig. 10 with the cruciform specimen highlighted in red. A clearer view of the centre of the specimen is presented in Fig. 11. Elastic cords (not shown) were used to suspend the weight of the hydraulic fixture. The configuration B tests used a similar test rig which differed in that the 4-point bending setup has been rotated by 90° around the vertical axis from configuration A. This brought about the aforementioned rotation of the coordinate system of P_x, P_y and P_z. The loading pins were mounted on cantilevers to provide horizontal compliance and avoid applying unintended bending on the specimen. Validation tests, measuring strain in the arms of the specimen, showed that less that 15% of load from the horizontal actuator was lost due to traction at the loading pins. Specimens were oriented such that at least one starter notch would be positioned at location 'a', 'b', 'e', or 'f' to avoid load lost from traction.

Strain gauges were applied to most specimens in both loading configurations. Each specimen had up to 12 gauges, arranged in pairs (one on each side) at six locations, as shown in Fig. 12. All gauges were connected in a half-bridge configuration. During testing, sites 1–4 were primarily used to measure bending strain, while sites 5 and 6 measured tensile strain.

Experimental strain data was examined to confirm that bending loads were applied as intended. Fig. 13 shows strain readings from test B1 at site 1, where gauges were arranged in a half-bridge bending arrangement. Test B1 was the third conducted using the B configuration of the test rig, where the cyclic bending stress and the tensile stress exerted by the hydraulic cylinder act on the same axis. FEA predicts a maximum and minimum strain of ±703.5 microstrain under fully reversed loading. The moving average line indicates that the mean strain during the test was −80 microstrain, while the strain amplitude was approximately 700 microstrain. The −80 microstrain offset likely resulted from an unintended bending load introduced by the hydraulic fixture. This offset was eliminated in subsequent tests by adjusting the tightness of the nuts in the hydraulic cylinder fixture prior to each test.

4. Results

4.1. Overview

The crack trajectory, which could be measured from the fracture surface after the completion of tests, was the primary output of interest. Surface maps of the crack faces were generated using an optical microscope. The crack growth rates of some of the specimens were calculated from striation spacing, visualised using a scanning electron microscope (SEM).

An overview of the test results is presented in Table 2.

4.2. Overview of results

Example crack trajectories from three specimens (A1, B5, B8) are presented in Figs. 14–16. A1 and B8 display the extremes of the crack trajectories which were produced in these series of tests. The crack trajectories of all completed tests have been previously reported in [19].

A1–A5 are considered to have the 'flattest' trajectories of the Ti-6Al-4V specimens tested. This is expected due the low ratio of hoop load to blade loads. In test configuration A, specimens were tested with cyclic blade loads and constant hoop loads, so trajectories closer to blade-wise were encouraged. Fig. 14a displays the surface of the crack face. A pattern of bright spots is caused by the microscope spotlight and the procedure of stitching an array of images. The texture of surfaces of the UD-rolled Ti-6Al-4V specimens was found to be highly faceted. From optical microscope images, it has not been possible to observe the typical indicators of a fatigue crack growth such as striations, beach marks, or river marks. However, as mentioned in the analysis of A2, striations are present and visible on the crack faces when imaged with SEM. A textural change is seen in the upper-left region near the shear lip at the top edge, which suggests that the final failure occurred here via fast fracture and that the largest crack grew from the lower-right corner. In Fig. 14b, the greatest deflection in z can be seen on the lower edge, which indicates crack initiation from at least one lower corner and minor deflection due to the hoop load. This is plotted in Fig. 14c on the plane $y = -7.50$ mm, which is close to the lower surface.

B5 was subjected to a greater hoop/blade load ratio and the hoop load was cycled according to the configuration B loading block as described in Section 3. It displays a larger kink angle and propagates at an angle large enough that the final failure occurs between two opposite internal corners. Despite the faceted appearance, several changes in texture are visible on the crack surface which outline the progression of the crack front. A prominent beach mark is also present which may indicate a large overload.

B8 was loaded with the greatest hoop/blade load ratio among all load schedules. Failure occurred due to crack growth between the starter notch and an adjacent corner with growth following the z-direction. This may be considered to be akin to a failure of a blisk due to crack growth in the hoop direction. A large number of ratchet marks are present around the starter notch. As expected, the ratchet marks point towards the point of crack initiation. Since the EDM notch raises stresses along its entire length, multiple cracks have initiated and merged together.

The initial growth angles of the resulting cracks are compared to predictions from MTS in Fig. 17. The load paths used in configuration A tests have resulted in flatter trajectories, which are closer to the trajectories expected of cracks driven by cyclic bending loads. In configuration B tests, the increased magnitude and infrequent cycling of P_z has had a greater influence on the trajectories. This effect is not correctly predicted by MTS. Of the configuration B tests, the relative error of the MTS prediction is lower in B8, as the hoop load is the main driver of crack growth due to the notch location and high ratio of P_z/P_y.

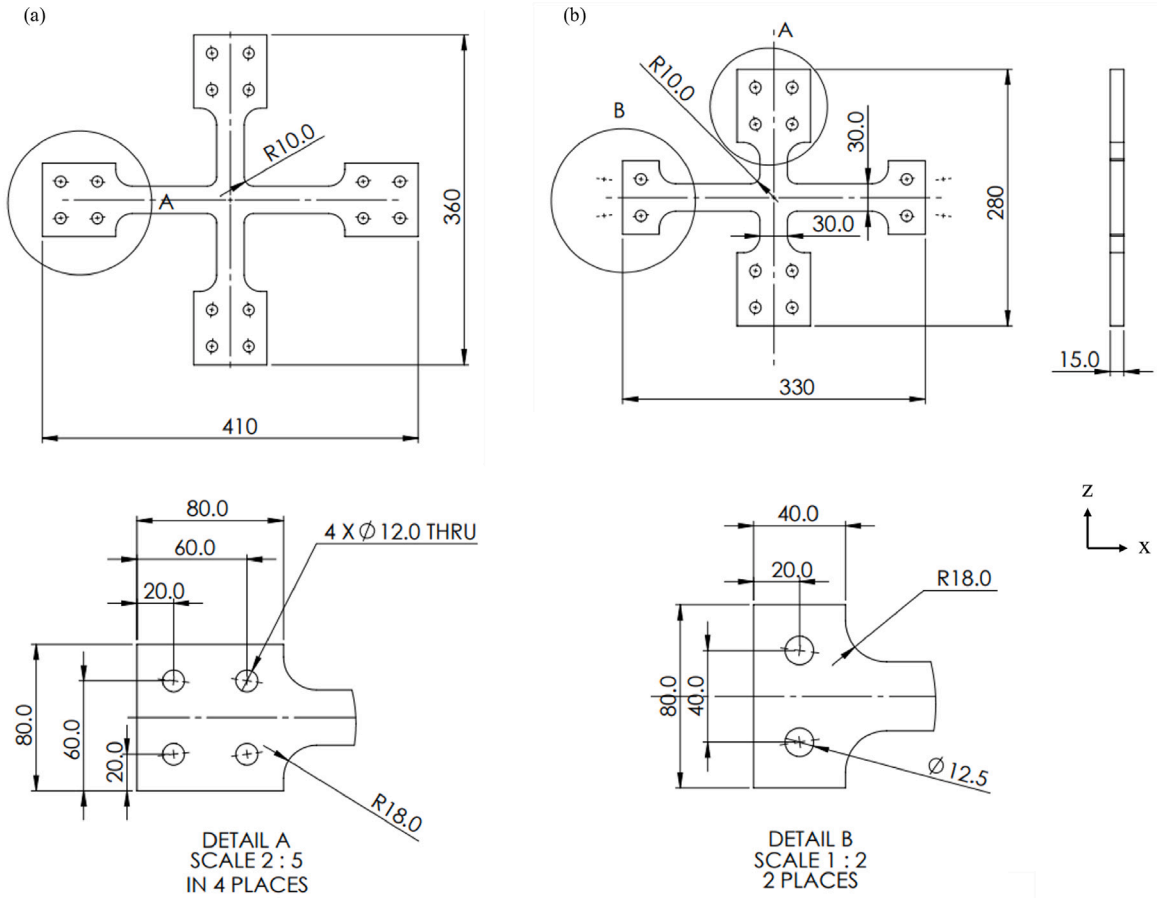


Fig. 8. Cruciform A and B schematic.

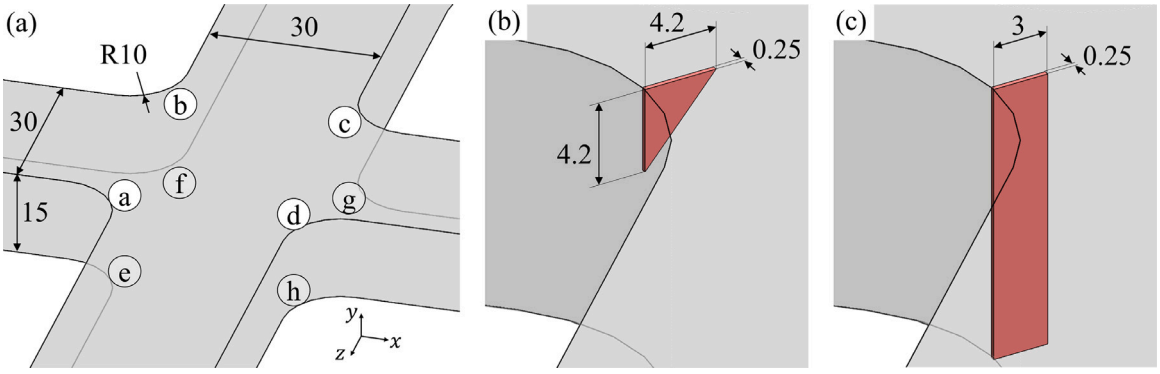


Fig. 9. (a) Notch locations. Dimensions of (b) corner notch at location 1 and (c) edge notch at location 1.

4.3. SEM striation counting

The number of cycles to failure, N_f, has varied significantly between specimens due to the absence of pre-cracks. Consequently, the cracks have spent a significant proportion of their lifetime in the initiation stage, resulting in values of N_f which do not correspond to propagation life. The direction and rate of fatigue crack growth in failed specimens were measured through striation counting.

SEM images of the fracture surface of some specimens have been taken at several points to compare crack growth rates with the MTS model. The results of A2, B5 and B8 are presented to compare the effectiveness of ΔK_I-based growth rate predictions for each load path.

4.4. Specimen A2

A series of SEM micrographs were captured at locations along the specimen edge to compare the crack growth rate calculated from striation spacing to that predicted by a simulated crack. The Walker model has been found to provide reasonable fatigue life predictions using a Walker fitting constant, $\gamma = 0.50$ to 0.54 [21,22]. Paris growth law constants ($C_0 = 1.07 \times 10^{-11}, m = 3.35$[1]) have been determined from previously completed crack growth rate tests. The tensile stress in the

[1] With K measured in MPa$\sqrt{\text{m}}$ and da/dN in mm/cycle.

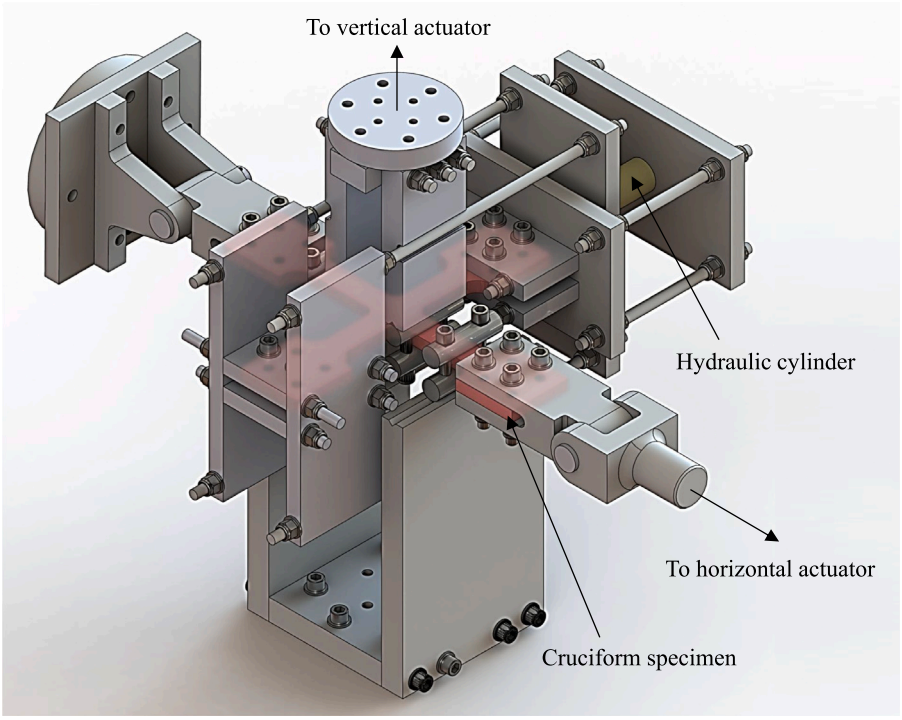


Fig. 10. Test rig configuration A.

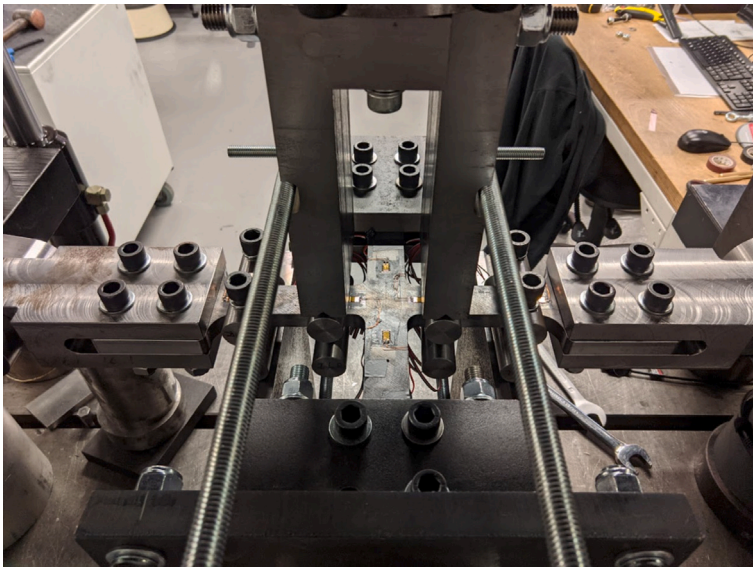


Fig. 11. Cruciform specimen and loading arms.

cruciform in the z-direction is summed from the effects of the bending load (R = −1) and tensile loads applied in the y and z-axes respectively. Because of this, the effective R-ratio at the surfaces of the specimen may be considered to be −0.60. The trajectories of the simulated cracks were determined by the MTS criterion. The cracks were modelled as simultaneously initiating and growing at equal rates and SIFs at the surface were recorded at the relevant locations.

The comparison of the ΔK_I values in Table 3 shows a very strong correlation between the prediction and experimental data. The locations listed in Table 3 are labelled in Fig. 18. It should be noted that locations sampled near $x = 0$ are not well aligned to the MTS due to asymmetry of the cracks in the specimen. At location F, the predicted value of ΔK_I is that of the midpoint where both cracks are modelled to coalesce. The assumption of small scale yielding is invalid in at this site due to the thinness of the remaining ligament when the crack reaches this region. Excluding the reading at F, ΔK_I has been compared with an average difference of 7.5%.

4.5. Specimen B5

Striation spacing values from the locations labelled in Fig. 19 are listed in Table 4. All locations were at $y = -7.0$ mm, which is 0.5 mm from the lowest point of the crack front, where it reaches the lower flat face of the cruciform. As expected from the non-proportional load paths, the features such as striations on the crack surface were broken up due the rubbing of crack faces. This was especially true near the starter notch, where no striations appeared to be present. Predicted

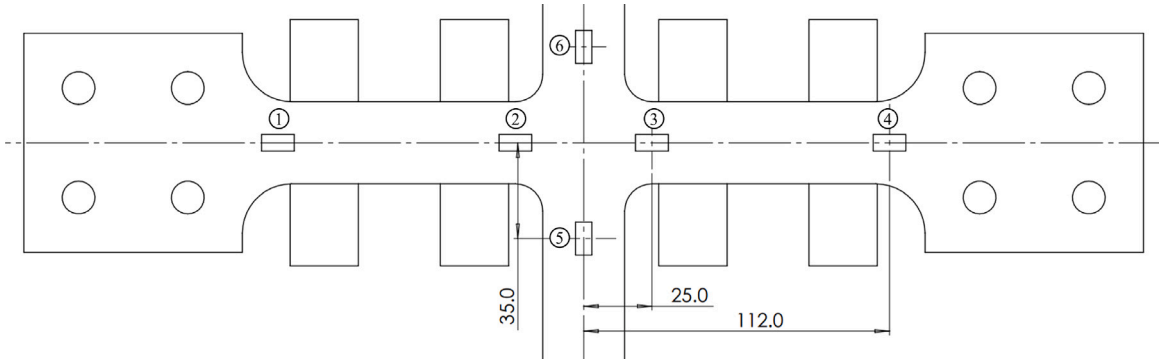


Fig. 12. Locations of strain gauges.

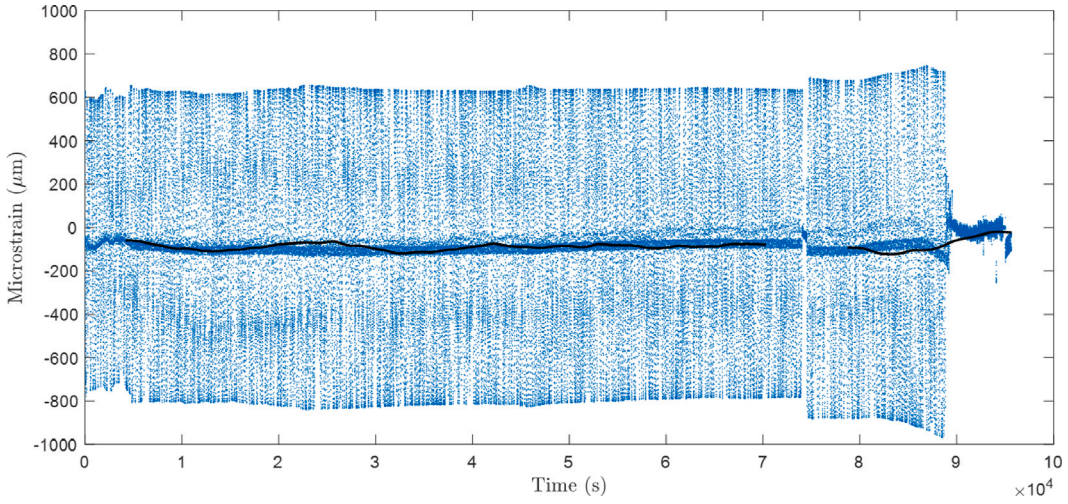


Fig. 13. Bending stress data recorded during test B1.

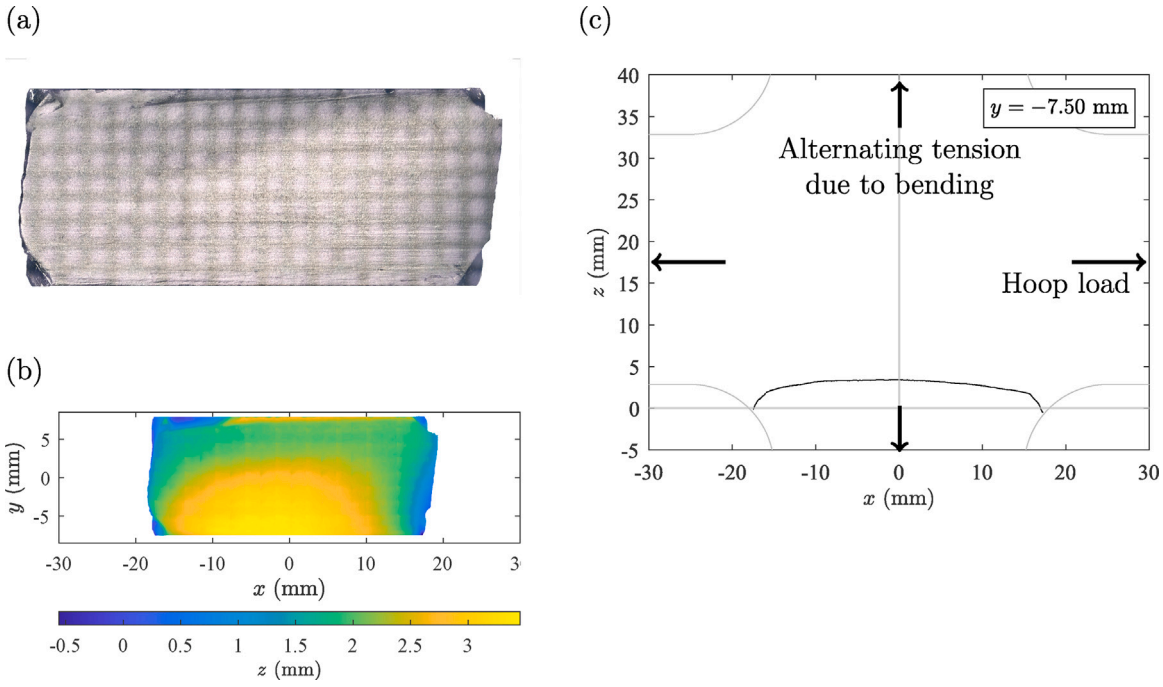


Fig. 14. Specimen A1 (a) crack face texture, (b) depth measurement and (c) crack trajectory at the free surface of the specimen.

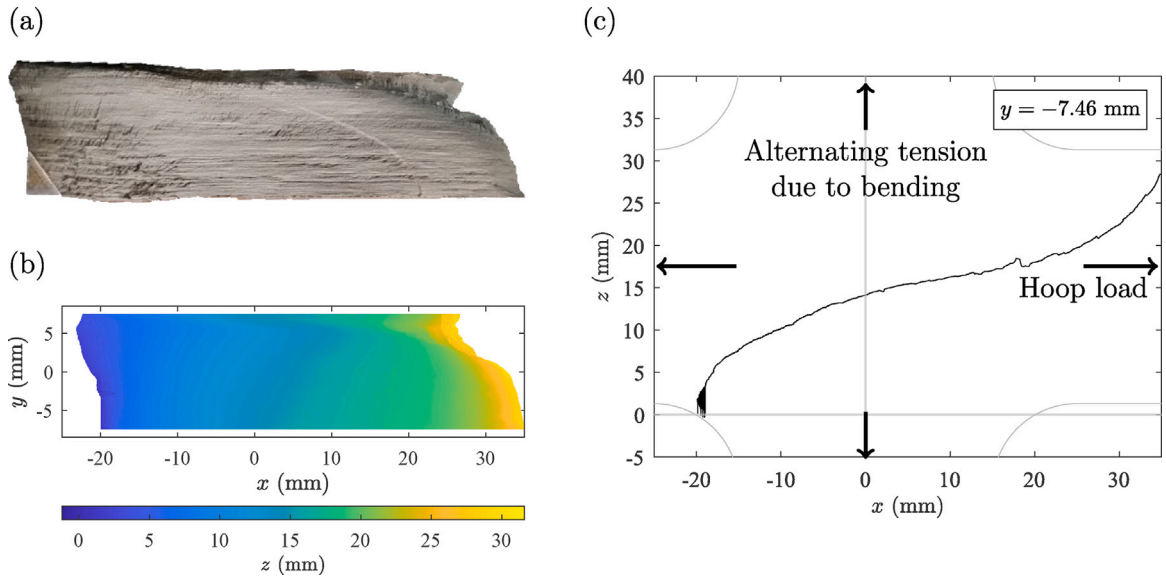


Fig. 15. Specimen B5 (a) crack face texture, (b) depth measurement and (c) crack trajectory at the free surface of the specimen.

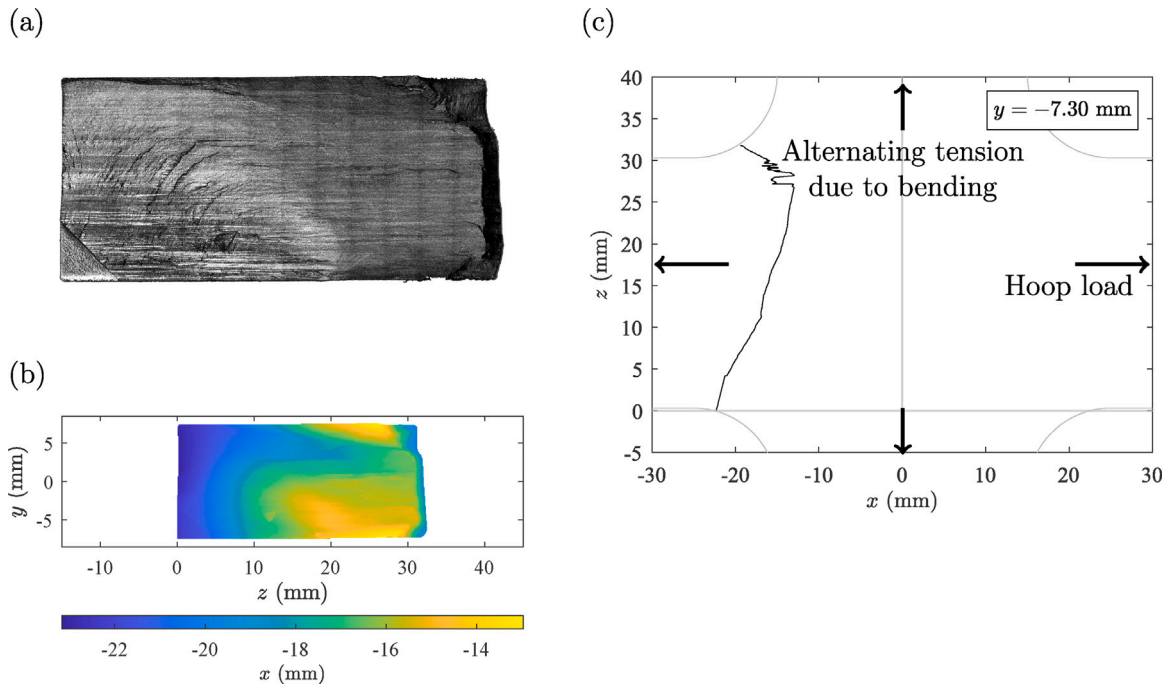


Fig. 16. Specimen B8 (a) crack face texture, (b) depth measurement and (c) crack trajectory at the free surface of the specimen.

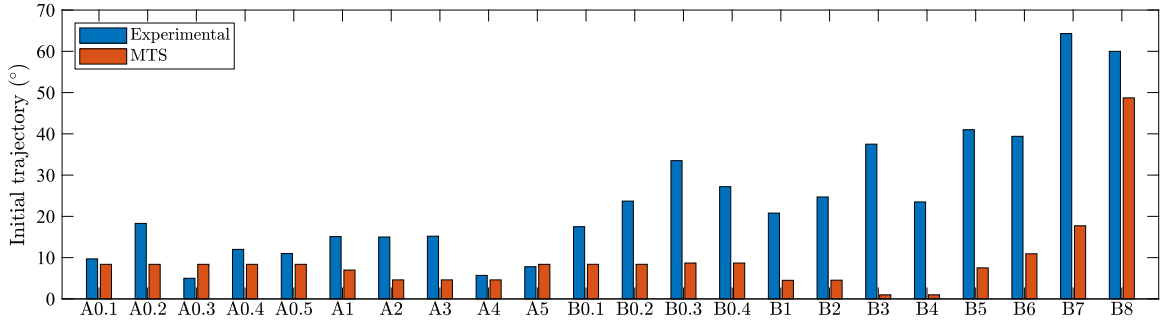


Fig. 17. Crack trajectory angles measured from x-axis.

Table 2
Overview of test results.

Test number	Material	Load (kN)				Number of notches	Nf	Initial angle, θ (°)
		P_x (R_x = 1)	P_y (R_y = −1)	P_z	R_z			
A0.1	S275	8.7	14.5	30.1	1	8C (Corner)	500,884	9.7
A0.2	S275	15.4	9.67	20.1	1	4E (Edge)	839,458	18.3
A0.3	S275	15.4	9.67	13.4	1	4E	1,614,217	5
A0.4	S275	15.4	9.67	13.4	1	2E	2,038,234	16.1, 8.2
A0.5	S275	15.4	9.67	13.4	1	2E	1,396,228	11
A1	Ti-6Al-4V	8.7	14.5	20.1	1	8C	261,306	15.1
A2	Ti-6Al-4V	15.4	9.67	20.1	1	4E	72,400	15
A3	Ti-6Al-4V	15.4	9.67	20.1	1	1E	867,347	15.2
A4	Ti-6Al-4V	15.4	9.67	13.4	1	2C	1,489,974	5.7
A5	Ti-6Al-4V	15.4	9.67	10.1	1	2C	3,464,933	7.8
B0.1	S275	8.7	9.67	50	0	1C	1,733,061	17.5
B0.2	S275	8.7	9.5	50	0	1C	1,530,000	23.7
B0.3	S275	8.7	5	80	0	1C	5,247,600	33.5
B0.4	S275	8.7	5	80	0	1C	3,436,000	27.2
B1	Ti-6Al-4V	8.7	9.5	50	0	1C	725,577	20.8
B2	Ti-6Al-4V	8.7	9.5	80	0	1C	588,200	24.7
B3	Ti-6Al-4V	8.7	5	80	0	1C	3,313,099	37.5
B4	Ti-6Al-4V	8.7	5	80	0	1C	4,016,600	23.5
B5	Ti-6Al-4V	8.7	9.5	80	0	1C, 60°	1,367,756	41
B6	Ti-6Al-4V	8.7	5	90	0	1C, 60°	4,354,000	39.4
B7	Ti-6Al-4V	8.7	10	80	0	1C, 75°	974,000	64.3
B8	Ti-6Al-4V	8.7	6	90	0	1C, 75°	2,848,800	60

Table 3
Comparison of ΔK_I at stages of crack growth in A2.

Location	x (mm)	y (mm)	Striation spacing (μm)	Experimental ΔK_I (MPa$\sqrt{m}$)	Predicted ΔK_I (MPa$\sqrt{m}$)
A	−14.04	7.21	0.082	17.9	19.9
B	−12.4	6.92	0.157	21.7	19.9
C	−8.03	6.62	0.180	22.6	22.5
D	−2.93	7.1	1.059	38.4	40.2
E	−2.74	7.16	1.785	44.9	40.8
F	−2.02	6.72	0.865	36.2	48.5
G	11.33	5.96	0.206	23.5	21

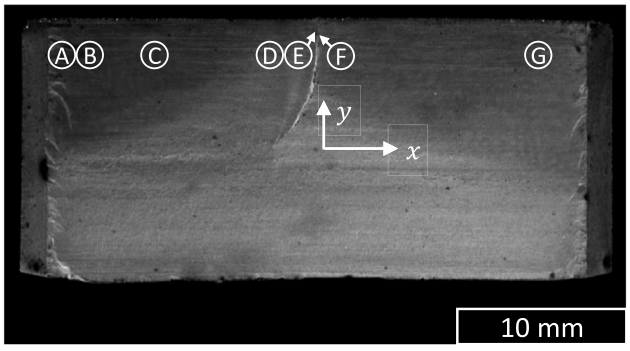


Fig. 18. Locations of striation measurements in A2.

values of ΔK_I have not been provided due to difficulties in simulating a crack of a similar shape.

The presence of striations and their spacing yields reasonable values of ΔK_I. At the point of crack initiation, the values of ΔK_{eff} from P_y and P_x are expected to be 3.73 MPa$\sqrt{m}$ and 9.39 MPa$\sqrt{m}$ respectively. Based on the Paris law constants, it may be concluded that P_y, which undergoes 200 cycles per block, drives crack growth despite the lower value of ΔK_{eff}.

The growth rate was expected to increase with the crack length due to the reduction of the remaining ligament. While this was generally true, the highest growth rate was measured at site C, where $x = 0$ mm, which is also where the trajectory in Fig. 15c is flattest and closest to the direction normal to the bending stress created by P_y. This further indicates that crack growth was predominantly driven by P_y.

A prominent beach mark is visible on the surface of B5 in Fig. 15a at $x = 24.7$ mm. It is not known if this is the result of an overload. Striations were counted on either side of this beach mark and the striation spacing was found to decrease across it from 0.140 μm to 0.092 μm between sites F and G crack growth retardation following an overload.

4.6. Specimen B8

Results of striation counting on specimen B8 are reported in Table 5 and measured sites are labelled in Fig. 20. As with specimen B5, striations were not visible in the area near to the starter notch. Throughout the rest of the fracture surface, striations were less intact than with previous specimens. Sites A-D are located near to the lower flat surface of the cruciform. Sites E and F are located at the left of the crack face in Fig. 16, positioned near to the round, filleted face of the cruciform. Striations at sites E and F are less damaged than at other sites. This is likely due to the fact that crack trajectory is almost normal to x and the crack opening due to P_x is greatest at sites E and F, so they are less affected by crack face rubbing during the cycling of P_y. The crack growth rate across sites B to D increased with the crack size, however the magnitude of the estimated experimental ΔK_I is of a larger magnitude than expected. At the starter notch, the values of ΔK_{eff} from P_y and P_x are simulated to be 1.24 MPa$\sqrt{m}$ and 12.7 MPa$\sqrt{m}$ respectively. It is also worth noting that the contribution of P_x is predominantly mode-I the contribution of P_y is predominantly mode-II. It is possible that P_x drives crack growth in this example since the contribution of P_y falls below the fatigue threshold. In test B8, P_y gives rise to a significant ΔK_{III} contribution which is 31% greater than its contribution of ΔK_I. The interaction of the large opening load of P_x with the mode-I and III components of P_y may explain the underestimation of growth rate by the model. However, taking measures to account for these such as ΔK_{eff} and Walker's model does not eliminate the discrepancy.

Table 4
Comparison of ΔK_I at stages of crack growth in B5.

Location	x (mm)	y (mm)	Striation spacing (μm)	Experimental ΔK_I (MPa$\sqrt{\text{m}}$)
A	−15.0	−7.0	n/a	n/a
B	−10.0	−7.0	0.051	15.5
C	0.0	−7.0	0.174	22.4
D	10.0	−7.0	0.115	19.8
E	20.0	−7.0	0.092	18.5
F	24.0	−7.0	0.140	21.0
G	25.0	−7.0	0.062	16.5
H	30.0	−7.0	0.289	26.1

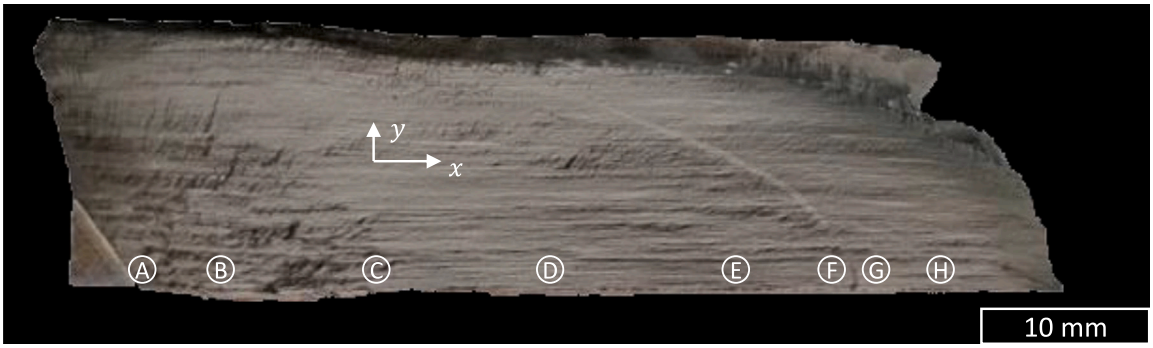


Fig. 19. Locations of striation measurements in B5.

Table 5
Comparison of ΔK_I at stages of crack growth in B8.

Location	z (mm)	y (mm)	Striation spacing (μm)	Experimental ΔK_I (MPa$\sqrt{\text{m}}$)
A	−15.0	−5.5	n/a	n/a
B	−10.0	−5.5	2.049	46.8
C	−5.0	−5.5	2.192	52.0
D	−0.2	−5.5	3.297	53.9
E	−18.5	−1.6	1.437	42.1
F	−18.5	3.2	0.611	32.6

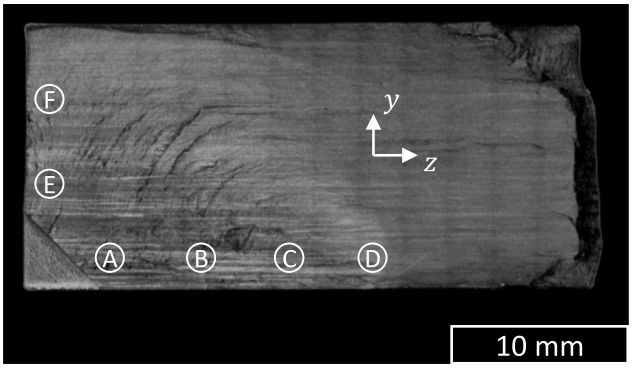


Fig. 20. Locations of striation measurements in B8.

5. Conclusions

A biaxial test rig was developed to conduct multiaxial fatigue tests on cruciform specimens in order to replicate loading conditions in a blisk and crack growth. Blade vibration in the "first flap" mode was identified as the primary driver of crack propagation due to the cyclic bending stresses that it exerted on the fillet region. However, the hoop stresses induced by rotational loading during operation of the engine were considered to be influential on the growth trajectory. Radial stresses from rotational loading also had a minor influence on crack growth.

The range of physically feasible trajectories of a crack initiating at the fillet of a cruciform can be assumed to span approximately 90°. This range represents a hypothetical spectrum of cracks in a blisk — spanning from a crack that grows across a blade whose trajectory is influenced only by first flap vibration, to a crack that grows towards the bore of the blisk under the influence of hoop loads. The range of initial crack trajectories spanned 60°. The angular range of crack front locations before the point of fracture is larger. Additionally, failure of cruciform specimens results from crack growth and fracture between the corner that the crack initiated from and one of the three other internal corners. Failures has been achieved between all three combinations of corners during the test campaign. So it can be concluded that the test setup has succeeded in producing an adequate range of crack trajectories under non-proportional loading conditions. Striation spacing was used to calculate the crack growth rate at several points of the test. Results matched very well with Paris-law based predictions in tests where cyclic bending stresses dominated crack growth. Growth rates differed greatly from predictions in tests with higher proportions of hoop loads.

CRediT authorship contribution statement

Bemin Sheen: Writing – original draft, Investigation. **Catrin Davies:** Supervision. **David Nowell:** Writing – review & editing, Supervision, Methodology, Funding acquisition, Conceptualization.

Declaration of competing interest

The authors declare that they have no known competing financial interests or personal relationships that could have appeared to influence the work reported in this paper.

Acknowledgements

The authors acknowledge EPSRC and Rolls-Royce for funding. The authors would like to thank Paul Mason, Rolls-Royce for his support.

Data availability

Data will be made available on request.

References

[1] Murakami Y, Fukushima Y, Toyama K, Matsuoka S. Fatigue crack path and threshold in Mode II and Mode III loadings. Eng Fract Mech 2008;75(3–4):306–18. http://dx.doi.org/10.1016/j.engfracmech.2007.01.030, URL https://linkinghub.elsevier.com/retrieve/pii/S0013794407001026.

[2] Qian J, Fatemi A. Mixed mode fatigue crack growth: A literature survey. Eng Fract Mech 1996;55(6):969–90. http://dx.doi.org/10.1016/S0013-7944(96)00071-9, URL https://linkinghub.elsevier.com/retrieve/pii/S0013794496000719.

[3] Richard HA, Fulland M, Sander M. Theoretical crack path prediction. Fatigue Fract Eng Mater Struct 2005;28(1–2):3–12. http://dx.doi.org/10.1111/j.1460-2695.2004.00855.x, URL https://onlinelibrary.wiley.com/doi/10.1111/j.1460-2695.2004.00855.x.

[4] Rozumek D, Macha E. A survey of failure criteria and parameters in mixed-mode fatigue crack growth. Mater Sci 2009;45(2):190–210. http://dx.doi.org/10.1007/s11003-009-9179-2, URL http://link.springer.com/10.1007/s11003-009-9179-2.

[5] Erdogan F, Sih GC. On the crack extension in plates under plane loading and transverse shear. J Fluids Eng Trans ASME 1963;85(4):519–25. http://dx.doi.org/10.1115/1.3656897.

[6] Rice JR. A path independent integral and the approximate analysis of strain concentration by notches and cracks. J Appl Mech 1968;35(2):379–86. http://dx.doi.org/10.1115/1.3601206, URL https://asmedigitalcollection.asme.org/appliedmechanics/article/35/2/379/392117/A-Path-Independent-Integral-and-the-Approximate.

[7] Iida S, Kobayashi AS. Crack-propagation rate in 7075-T6 plates under cyclic tensile and transverse shear loadings. J Basic Eng 1969;91(4):764–9. http://dx.doi.org/10.1115/1.3571219, URL https://asmedigitalcollection.asme.org/fluidsengineering/article/91/4/764/397666/CrackPropagation-Rate-in-7075T6-Plates-Under.

[8] Borodii MV. Determination of the non-proportional cyclic hardening coefficient sensitive to the loading amplitude. Strength Mater 2020;52(6):919–29. http://dx.doi.org/10.1007/s11223-021-00245-7, URL http://link.springer.com/10.1007/s11223-021-00245-7.

[9] Skibicki D, Pejkowski L. The relationship between additional non-proportional hardening coefficient and fatigue life. Int J Fatigue 2019;123:66–78. http://dx.doi.org/10.1016/j.ijfatigue.2019.02.011, URL https://linkinghub.elsevier.com/retrieve/pii/S0142112319300404.

[10] Kang G, Li Y, Gao Q. Non-proportionally multiaxial ratcheting of cyclic hardening materials at elevated temperatures: Experiments and simulations. Mech Mater 2005;37(11):1101–18. http://dx.doi.org/10.1016/j.mechmat.2005.01.006, URL https://linkinghub.elsevier.com/retrieve/pii/S0167663605000608.

[11] Shamsaei N, Fatemi A, Socie DF. Multiaxial fatigue evaluation using discriminating strain paths. Int J Fatigue 2011;33(4):597–609. http://dx.doi.org/10.1016/j.ijfatigue.2010.11.002, URL https://linkinghub.elsevier.com/retrieve/pii/S0142112310002665.

[12] Shamsaei N, Fatemi A. Small fatigue crack growth under multiaxial stresses. Int J Fatigue 2014;58:126–35. http://dx.doi.org/10.1016/j.ijfatigue.2013.02.002.

[13] Yu X, Li L, Proust G. Fatigue crack growth of aluminium alloy 7075-T651 under proportional and non-proportional mixed mode I and II loads. Eng Fract Mech 2017;174:155–67. http://dx.doi.org/10.1016/j.engfracmech.2017.01.008.

[14] Mangardich D, Abrari F, Fawaz Z. Modeling crack growth of an aircraft engine high pressure compressor blade under combined HCF and LCF loading. Eng Fract Mech 2019;214(April):474–86. http://dx.doi.org/10.1016/j.engfracmech.2019.04.028, URL https://linkinghub.elsevier.com/retrieve/pii/S0013794418312785.

[15] Wawrzynek PA, Carter BJ, Ingraffea AR. Advances in simulation of arbitrary 3D crack growth using FRANC3D/NG. In: 12th International conference on fracture 2009, ICF-12. vol. 1, 2009, p. 344–54.

[16] Barlow KW, Chandra R. Fatigue crack propagation simulation in an aircraft engine fan blade attachment. Int J Fatigue 2005;27(10–12):1661–8. http://dx.doi.org/10.1016/j.ijfatigue.2005.06.016.

[17] Byrne J, Hall RF, Powell BE. Influence of LCF overloads on combined HCF/LCF crack growth. Int J Fatigue 2003;25(9–11):827–34. http://dx.doi.org/10.1016/S0142-1123(03)00131-2.

[18] Witek L. Simulation of crack growth in the compressor blade subjected to resonant vibration using hybrid method. Eng Fail Anal 2015;49:57–66. http://dx.doi.org/10.1016/j.engfailanal.2014.12.004.

[19] Sheen B. Trajectories of multiaxial non-proportional fatigue cracks: Experiment and simulation (Ph.D. thesis), Imperial College London; 2024.

[20] Ritchie R. Thresholds for high-cycle fatigue in a turbine engine Ti–6Al–4V alloy. Int J Fatigue 1999;21(7):653–62. http://dx.doi.org/10.1016/S0142-1123(99)00024-9, URL https://linkinghub.elsevier.com/retrieve/pii/S0142112399000249.

[21] Dowling NE. Mean stress effects in strain-life fatigue. Fatigue Fract Eng Mater Struct 2009;32(12):1004–19. http://dx.doi.org/10.1111/j.1460-2695.2009.01404.x.

[22] Carrion PE, Shamsaei N, Daniewicz SR, Moser RD. Fatigue behavior of Ti-6Al-4V ELI including mean stress effects. Int J Fatigue 2017;99:87–100. http://dx.doi.org/10.1016/j.ijfatigue.2017.02.013, Publisher: Elsevier Ltd.